


## PAPER

[View Article Online](#)  
[View Journal](#)

Cite this: DOI: 10.1039/d5dd00353a

**BRINE: a cost-effective electrochemical self-driving laboratory for accelerated discovery of high-performance electrolytes**Mohamadreza Ramezani, Poulomi Nandi, Pablo Antonio De La Fuente-Moreno and Majid Beidaghi \*

The discovery of next-generation battery electrolytes increasingly involves complex, multicomponent formulations that demand high-throughput, systematic exploration. We present the Bayesian Robotic Investigator of Novel Electrolytes (BRINE), a cost-effective, self-driving laboratory (SDL) that autonomously prepares and tests mixed electrolyte solutions. BRINE combines an open-source liquid-handling robot with a potentiostat and custom-made electrodes to mix reagents and perform electrochemical measurements without human intervention. A Bayesian optimization routine navigates multidimensional composition spaces, allowing the platform to rapidly identify promising formulations. As a proof of concept, BRINE mapped ionic conductivity in two aqueous electrolyte spaces (i) aqueous mixtures of NaCl, KCl, MgCl<sub>2</sub>, and CaCl<sub>2</sub>, and (ii) battery-oriented mixtures containing ZnCl<sub>2</sub>, KCl, NH<sub>4</sub>Cl, NaCl, and EMIMCl, testing  $\approx 230$  unique compositions in under 20 hours and finding conductivities up to 32.13 S m<sup>-1</sup>. These results demonstrate how closed-loop autonomous experimentation and optimization accelerate the identification of electrolytes with the highest conductivity across a large multicomponent composition space, while minimizing experimental variability. This work lays the foundation for broader electrochemical studies using the BRINE platform.

Received 8th August 2025  
Accepted 27th November 2025

DOI: 10.1039/d5dd00353a

[rsc.li/digitaldiscovery](https://rsc.li/digitaldiscovery)**Introduction**

Rapid advances in materials science and electrochemical technologies are driving demand for innovative experimental methodologies that can explore increasingly complex systems.<sup>1</sup> In electrochemical systems such as energy storage, electrochemical sensing, and electrocatalysis, the compositions of electrodes, electrolytes, and interfaces are increasingly multicomponent.<sup>2–4</sup> For example, high-entropy electrode materials, formed by combining five or more elements to maximize configurational entropy and stabilize host lattices, deliver higher capacity retention and longer cycle life in batteries, demonstrating the advantages of multi-component chemistries. Similarly, high-entropy electrolytes, which may contain multiple salts, solvents, and additives, can be tailored to engineer ion transport and interfacial properties, resulting in compositional spaces that far exceed what manual experimentation can feasibly sample.<sup>5,6</sup>

Although a variety of electrochemical methods are available to study the properties of electrolytes,<sup>7–13</sup> conventional approaches typically rely on sequential, manual protocols that are both time-consuming and prone to human error.<sup>14–16</sup> These limitations are exacerbated when investigating mixed

electrolyte or high-entropy formulations, where manual workflows struggle to cover combinatorial spaces and are prone to cross-contamination or measurement biases.<sup>17–21</sup> To overcome these bottlenecks, new automated platforms are needed to systematically prepare, measure, and analyze large numbers of electrolytes with minimal human intervention.

Recent developments in artificial intelligence, robotics, and electrochemical measurement methods have led to the development of electrochemical self-driving laboratories (SDLs) that overcome these traditional limitations.<sup>22–25</sup> Several advanced SDL platforms have been proposed in the literature, capable of synthesizing materials, performing electrochemistry, and leveraging machine learning algorithms to guide successive experiments.<sup>26–29</sup> However, many existing platforms depend on custom hardware, complex integration, and, in some cases, significant financial investment.<sup>30–33</sup> To address these limitations, we designed BRINE (Bayesian Robotic Investigator of Novel Electrolytes), a streamlined, cost-effective SDL tailored to high-throughput exploration of electrolytes. BRINE achieves high levels of autonomy using commercially available components,<sup>34</sup> providing accurate and rapid experimental results while lowering the barrier to entry.

Central to BRINE is the Opentrons OT-2 pipetting robot, chosen for its precision, affordability, and programmability. We modified the OT-2 to prepare electrolyte mixtures with sub-microliter accuracy, perform electrochemical measurements,

Department of Aerospace & Mechanical Engineering, The University of Arizona, Tucson, AZ 85721, USA. E-mail: [beidaghi@arizona.edu](mailto:beidaghi@arizona.edu)



and coordinate washing and drying cycles for the electrodes. BRINE uses a 3D-printed electrode assembly that houses platinum electrodes and interfaces with a potentiostat for electrochemical measurements. To showcase BRINE's capabilities in autonomously optimizing properties of complex electrolytes, we used it to maximize ionic conductivity in mixed electrolyte systems. While the performance of electrolytes depends on multiple parameters, ionic conductivity is among the most critical metrics considered in electrolyte design. However, current models for predicting the ionic conductivity of electrolytes cannot capture the combined effects of ion association, solvation structure, dielectric changes, and non-ideal mixing at moderate to high concentrations.<sup>20,35,36</sup> The classical Debye-Hückel-Onsager theory applies only to infinitely dilute binary salts, and later extensions tailored for specific binary or ternary systems depend on system-specific parameters, thereby missing the nonlinear, non-additive behavior observed in multi-component electrolytes.<sup>35–37</sup> Thus, we selected the problem of maximizing ion conductivity of a mixed multi-component electrolyte to demonstrate the functionality and advantages of BRINE.

The entire BRINE workflow, from sample preparation and measurement to data analysis and experimental redesign, is orchestrated by a Bayesian optimization (BO) engine.<sup>38,39</sup> This engine balances exploration and exploitation, sequentially proposing new electrolyte compositions predicted to maximize ionic conductivity, while simultaneously improving the underlying Bayesian surrogate model by updating its understanding of how composition affects conductivity.

BRINE leverages minimal hardware and open-source software to deliver high-throughput electrochemical measurements while showing a Level 4 autonomy.<sup>39</sup> Once an experimental campaign is initiated, BRINE autonomously selects, conducts, and analyzes experiments, ultimately updating its optimization strategy without human oversight. This closed-loop architecture minimizes human error, improves reproducibility, and accelerates convergence toward optimal formulations. Related efforts have demonstrated the use of robotic platforms for electrolyte screening. For example, Yik *et al.* introduced ODA-Cell and its successor ODACell 2, which integrate automated coin-cell assembly, robotic handling, machine-vision guidance, and Bayesian optimization in a closed-loop framework to accelerate electrolyte discovery. These studies highlight the growing role of automation in electrolyte research while underscoring the need for accessible and modular platforms.<sup>40,41</sup> In parallel, a recent study by Lin *et al.*<sup>42</sup> described a similar platform for optimizing the coulombic efficiency of electrolytes for zinc-ion batteries. However, their platform relied on predefined experimental grids, whereas BRINE's Bayesian engine actively determines sampling locations, highlighting the distinction between high-throughput screening and true self-driving experimentation.

BRINE addresses longstanding challenges in electrochemical studies, including variability in manual preparation and slow throughput. By automating the preparation and electrochemical measurements of properties, it generates high-quality data that can feed machine learning models for

electrolyte discovery. While demonstrated here for optimization of ionic conductivity, the platform's modularity and closed-loop architecture pave the way for incorporating additional electrochemical measurements in future iterations, positioning BRINE as a versatile and accessible tool for the electrochemical research community.

## Chemicals and materials

All chemicals used were of analytical grade. Sodium chloride (NaCl,  $\geq 99.0\%$ ), potassium chloride (KCl,  $\geq 99.0\%$ ), magnesium chloride hexahydrate ( $\text{MgCl}_2 \cdot 6\text{H}_2\text{O}$ ,  $\geq 98.0\%$ ), calcium chloride dihydrate ( $\text{CaCl}_2 \cdot 2\text{H}_2\text{O}$ ,  $\geq 97.0\%$ ), zinc chloride ( $\text{ZnCl}_2$ ,  $\geq 98.0\%$ ), ammonium chloride ( $\text{NH}_4\text{Cl}$ ,  $\geq 99.5\%$ ), and 1-ethyl-3-methylimidazolium chloride (EMIMCl,  $\geq 98.0\%$ ) were obtained from Thermo Scientific chemicals and used as received without further purification. Deionized water (resistivity  $\geq 18.2 \text{ M}\Omega \text{ cm}$ ) was used as the solvent for all electrolyte solutions to ensure minimal contamination and consistent ionic behavior.

## Hardware and electrode fabrication

Our experimental setup combines electrochemical instrumentation, robotic automation, and custom-designed electrodes for fully autonomous testing. The Opentrons OT-2 robot, widely adopted for precise and reproducible liquid handling tasks, is incorporated at the core of the system. Liquid manipulation tasks, including aspiration, dispensation, mixing, electrode immersion, and washing, are executed through custom Python protocols.

We used an OT-2 Single-Channel P300 Gen2 pipette equipped with compatible 300  $\mu\text{L}$  pipette tips for accurate liquid handling. A Single-Channel P1000 Gen2 pipette was modified to handle our custom 3D-printed electrode, comprising two parallel platinum strips ( $\text{Pt} \parallel \text{Pt}$ ) with a defined liquid exposure area and an integrated cable holder (Fig. S1). The electrode assembly was mechanically attached to the P1000 pipette, ensuring synchronized movements and stable electrical connection *via* secured potentiostat cables.

Ionic conductivity of the electrolytes was measured using Electrochemical Impedance Spectroscopy (EIS) performed by a Gamry 1010E potentiostat in a two-electrode configuration, operated from 1.2 MHz to 5 kHz to precisely measure electrolyte resistance at high frequencies (above 100 kHz).<sup>43,44</sup> NEST 12-well, 15 mL reservoirs were used to store electrolyte stocks and electrode washing liquids (water and ethanol) on the BRINE platform. The ethanol reservoir was continuously topped off using an Aladdin AL-300 syringe pump. Electrolyte mixing and measurements were performed in NEST 96-well, 200  $\mu\text{L}$  plates. A 5 V DC fan facilitated rapid electrode drying post-washing.

## Protocols and specifications

### Electrolyte selection

BRINE's capability to find electrolyte compositions with maximum ionic conductivity was tested in two aqueous



electrolyte systems. Because this manuscript represents the first report of BRINE, the two campaigns were selected to demonstrate the platform's performance under complementary conditions. Campaign 1 employed a simple four-cation chloride system (NaCl, KCl, MgCl<sub>2</sub>, CaCl<sub>2</sub>) that is chemically tractable and allowed benchmarking of the optimizer's ability to balance monovalent and divalent species without additional complexities. Campaign 2, in contrast, was designed to highlight BRINE's practical relevance for energy storage by focusing on a Zinc-ion battery electrolyte space. Here we included ZnCl<sub>2</sub>, NH<sub>4</sub>Cl, NaCl, KCl, and EMIMCl, reflecting formulations actively investigated in zinc-ion and zinc-air battery systems. NH<sub>4</sub>Cl was incorporated due to its demonstrated ability to improve Zn electrolyte performance through buffering capacity, hydrogen-bonding-mediated transport, and stabilization effects.<sup>45–49</sup> EMIMCl (1-ethyl-3-methylimidazolium chloride) was added to represent functional additives commonly used in formulation of Zn-ion battery electrolytes rather than a conductivity enhancer.<sup>50–53</sup> Ionic liquids of this type are widely reported to suppress dendrite formation and promote uniform Zn deposition.<sup>54,55</sup> The electrolytes with specific composition were prepared by mixing aliquots from reservoirs that contained concentrated solutions of salts. The concentrations of salts in the reservoirs are summarized in Table S5.

### Labware preparation

Two 15 mL reservoirs were placed on the OT-2 deck. The first reservoir contained stock electrolyte solutions for automated aspiration; the second housed four wells filled with DI water and one well filled with ethanol to facilitate electrode washing and drying (Fig. S2). Tip racks and additional well plates were arranged as necessary.

### Ionic conductivity measurement and optimization

Ionic conductivity ( $\sigma$ , S m<sup>−1</sup>) was calculated using the empirical relationship (eqn (1)):<sup>10,43</sup>

$$\sigma = \frac{l}{AR} \quad (1)$$

where  $l$  (m) is the electrode gap,  $A$  (m<sup>2</sup>) is the effective electrode area, and  $R$  ( $\Omega$ ) is the measured solution resistance. To mitigate inaccuracies, we determined the electrode's cell constant ( $K_{\text{cell}} = l/A$ ) empirically rather than geometrically (Fig. S3). A Python-based circuit-fitting approach was employed to automatically extract electrolyte resistance from their Nyquist plots.<sup>56</sup>

The optimization goal for electrolyte mixtures was defined mathematically as follows (eqn (2a) and (2b)):

$$\max_{\{V_i\}} \sigma \quad (2a)$$

$$\text{s.t.} \begin{cases} V_i \geq 20 \text{ } \mu\text{L}, \\ \sum_{i=1}^N V_i \leq 330 \text{ } \mu\text{L}, \\ V_i \in \mathbb{N} \end{cases} \quad (2b)$$

Here,  $V_i$  denotes pipetting volumes of each electrolyte  $i$ ,  $N$  is the total electrolyte count, the first constraint reflects the minimum OT-2 pipette volume, the second constraint ensures no well plate overflow, and the integer constraint reflects pipetting practicality. Ambient conditions of approximately  $25 \pm 1$  °C and 10% RH were maintained consistently throughout all experiments to ensure reproducibility.

The closed-loop process involved four core sub-operations: (1) solution preparation, (2) electrochemical testing, (3) electrode washing and drying, and (4) data analysis with Bayesian optimization, as detailed in Fig. 1.

### Software integration and optimization strategy

Software and hardware coordination was provided by NIMS-OS,<sup>57</sup> an open-source orchestration system developed specifically for self-driving laboratories, offering centralized control of all hardware and software interfaces. Real-time communication between NIMS-OS and OT-2 employed a Python-based Web-Socket API,<sup>58</sup> superior to REST-based approaches due to real-time bidirectional data flow necessary for immediate experimental feedback loops.<sup>42,59</sup>

Considering the discrete, noisy, and constrained nature of our ionic conductivity optimization experiments, particularly those involving EIS, which is known for its indeterministic and non-smooth response characteristics, we implemented SMAC3 with a Random Forest (RF) surrogate model as the Bayesian optimizer.<sup>39,60</sup> RF was selected due to its superior handling of noise and discrete variables and its significantly lower computational complexity ( $O(n \log n)$ ) compared to Gaussian Processes ( $O(n^3)$ ), making it particularly suitable for our real-time closed-loop experiments. While Gaussian Process (GP) models excel in smooth, continuous domains and provide strong uncertainty quantification, their reliance on smoothness assumptions and poor scaling with sample size make them less effective under BRINE's discrete pipetting constraints and measurement variability. Prior studies also show that RF-based surrogate models can outperform GP-based approaches in applied noisy, multi-source datasets, further supporting this choice.<sup>61,62</sup>

To avoid prior bias, SMAC3 was initialized without prior data, using a structured three-phase acquisition strategy for balanced exploration and exploitation efficiency<sup>63–65</sup> as follows:

- Phase BEE (Balanced Exploration-Exploitation,  $\approx 50\%$  experiments): Alternating Expected Improvement (EI,  $\xi = 0$ ) and Lower Confidence Bound (LCB,  $\beta = 1.2$ ), to identify promising regions while ensuring global parameter-space coverage.
- Phase FE (Focused Exploitation,  $\approx 30\%$  experiments): Targeted local refinement within  $\pm 10$   $\mu\text{L}$  of previously optimal mixtures using EI ( $\xi = 0.05$ ) to sharpen local maxima.
- Phase GE (Global Exploration,  $\approx 20\%$  experiments): Predominantly global searches using LCB ( $\beta = 2.0$ ), occasionally interleaving EI ( $\xi = 0$ ) to revisit and refine promising regions.

This multi-stage curriculum allows transparent, reproducible, and budget-aware exploration of complex multi-modal search landscapes. Unlike adaptive black-box switching strategies (e.g., GP-Hedge), the staged SMAC3 approach provides



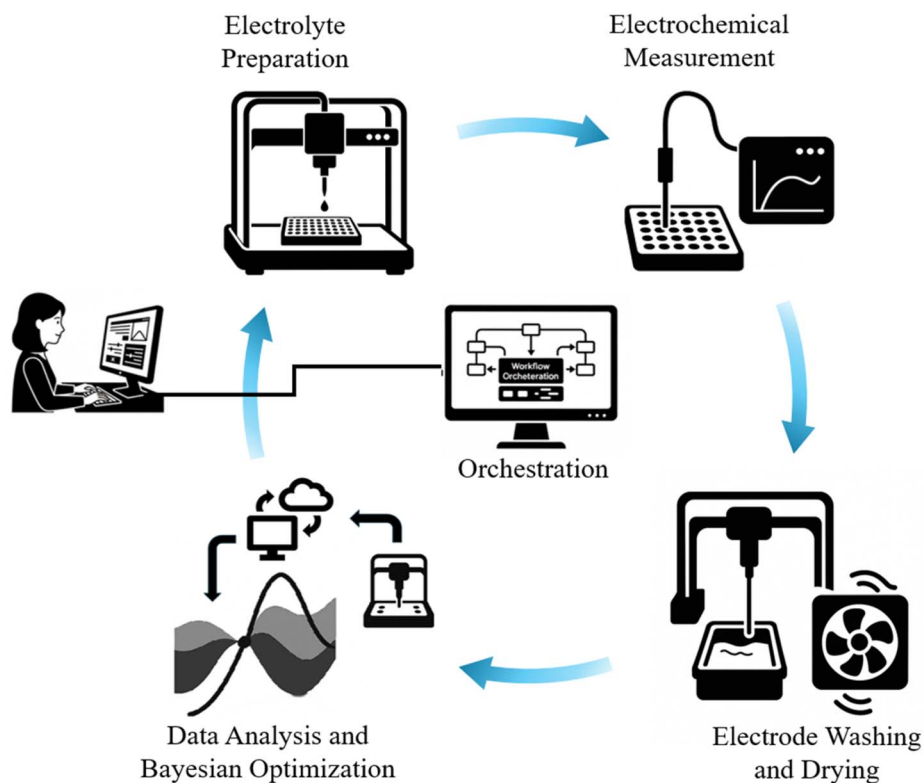


Fig. 1 Closed loop process breakdown. The SDL follows the 4 stages shown with an orchestration unit responsible for all the interactions between these components.

explicit control over exploration–exploitation scheduling, which is advantageous under strict experimental budgets.<sup>66</sup>

Classical Design of Experiments (DoE) methods such as Box–Behnken and D-optimal designs are highly effective for generating polynomial response surfaces, but they are not well-suited to the electrolyte design space studied here. The space is a discrete, mixture-constrained lattice dictated by pipetting increments ( $\geq 20 \mu\text{L}$ ) and total volume constraints ( $\leq 330 \mu\text{L}$ ), and ionic conductivity in concentrated multicomponent electrolytes is inherently nonlinear, non-additive, and multimodal with multiple local optima. These characteristics violate the assumptions underlying polynomial DoE models, necessitate redesign of infeasible DoE points, and cannot be fully encoded within classical DoE frameworks. For these reasons, a D-optimal design was used only as a baseline reference strategy to benchmark BRINE's Bayesian optimization performance.

#### Autonomous workflow for ionic conductivity optimization

With the necessary SDL components in place, we tasked BRINE with autonomously performing ionic conductivity measurements and optimizing the conductivity through the following iterative procedure (these steps are visualized in Fig. S4 and the SI Video-1):

Step 1 (system initialization): each iteration begins with calibration of the OT-2 robot's pipette and the electrode setup positions, ensuring accurate subsequent operations.

Step 2 (electrolyte preparation): based on conditions proposed by BO, the robot aspirates the specified electrolyte

volumes from the stock reservoir and dispenses them into the target well. For the initial experiment, where no prior data exists, the BO employs a constrained random sampling strategy.<sup>60</sup> Pipette tips are replaced after each aspiration–dispense cycle to prevent cross-contamination. Following electrolyte addition, thorough mixing is achieved by repeatedly aspirating and dispensing  $150 \mu\text{L}$  of the solution four times, ensuring solution uniformity. Prior to each campaign, preliminary solubility assessments were performed to establish upper concentration limits for each salt, and these values were used to define the optimizer's search constraints. After each campaign, the wells were carefully inspected and no precipitation or phase separation was observed, confirming that all mixtures remained homogeneous during conductivity measurements.

Step 3 (electrochemical measurement): the electrode assembly is carefully immersed in the prepared solution, fully submerging the designated active area of the electrode strips. Ionic conductivity measurement (*via* EIS) is then automatically initiated.

Step 4 (electrode cleaning and drying): after measurement completion, the electrode undergoes automated washing in DI water and ethanol (Fig. S2), followed by drying facilitated by airflow from a 5 V fan.

Step 5 (data analysis and optimization): conductivity data is relayed to the orchestration unit, stored systematically, and subsequently analyzed by the Bayesian optimizer. Based on trends from the updated dataset, the Bayesian optimizer proposes the next experimental conditions, initiating the subsequent iteration.





## Results and discussion

### Campaign findings

The room temperature ionic conductivities of the four stock electrolytes are plotted in Fig. 2. Across their respective solubility limits, KCl displays the highest conductivity, rising monotonically to  $\approx 33 \text{ S m}^{-1}$  at 4 M. NaCl follows a similar upward trend, reaching  $\approx 22 \text{ S m}^{-1}$  near 5 M. In contrast,  $\text{CaCl}_2$  exhibits a conductivity maximum ( $\approx 21 \text{ S m}^{-1}$ ) at  $\approx 3.5 \text{ M}$  before declining slightly, consistent with viscosity-induced transport limitations at higher concentrations.  $\text{MgCl}_2$  remains the poorest conductor throughout the tested range, plateauing below  $17 \text{ S m}^{-1}$  even at 4 M. These baseline measurements are consistent with the reported ionic conductivities of these solutions<sup>21,67,68</sup> and establish a reference for interpreting the Bayesian-optimized mixtures discussed in subsequent sections, while explaining why KCl-rich formulations frequently dominate the conductivity maxima identified by BRINE.

We tested BRINE's capability in maximizing the ionic conductivity of mixed electrolytes in two experimental campaigns. The first closed-loop campaign comprised 114 experiments executed in three sequential phases: Balanced Exploration–Exploitation (BEE, 61 runs), Focused Exploitation (FE, 30 runs), and Global Exploration (GE, 23 runs). For each composition, a single mixture was prepared, and EIS measurements were performed three times consecutively; the average of the three results was reported. The entire campaign was

completed in  $\approx 10 \text{ h}$ , underscoring the high-throughput capability of the platform.

Fig. 3 shows both the evolving salt concentrations and the ionic conductivity of the tested electrolytes. During the BEE phase, the Bayesian optimizer sampled broadly, confirming that NaCl and KCl dominate conductivity while  $\text{MgCl}_2$  contributes negligibly. Once this trend was captured by the surrogate model, the algorithm entered the FE phase, converging to a narrow region rich in NaCl and KCl. The subsequent GE phase intentionally perturbed the search space to check for missed global optima and improve model uncertainty. The highest conductivity recorded was  $32.12 \text{ S m}^{-1}$ , an electrolyte composed of 2.05 M NaCl/1.61 M KCl/0.09 M  $\text{MgCl}_2$ /0.22 M  $\text{CaCl}_2$  ( $\pm 0.10 \text{ M}$  precision). The second-best conductivity ( $31.48 \text{ S m}^{-1}$ ) was for an electrolyte which contained 0.42 M NaCl, 1.77 M KCl, 0.09 M  $\text{MgCl}_2$  and 1.04 M  $\text{CaCl}_2$ . Both high-performing compositions contained significant amounts of KCl. However, the top-performing composition was primarily dominated by NaCl, whereas the second one had  $\text{CaCl}_2$  as the secondary dominant electrolyte.  $\text{MgCl}_2$  consistently had minimal influence, as evidenced by the BO minimizing its concentration.

While Campaign 1 demonstrated BRINE's ability to maximize conductivity in an unconstrained, four-salt system, practical battery electrolytes often require a minimum concentration for specific ions. To test BRINE under such application-driven constraints, we designed Campaign 2

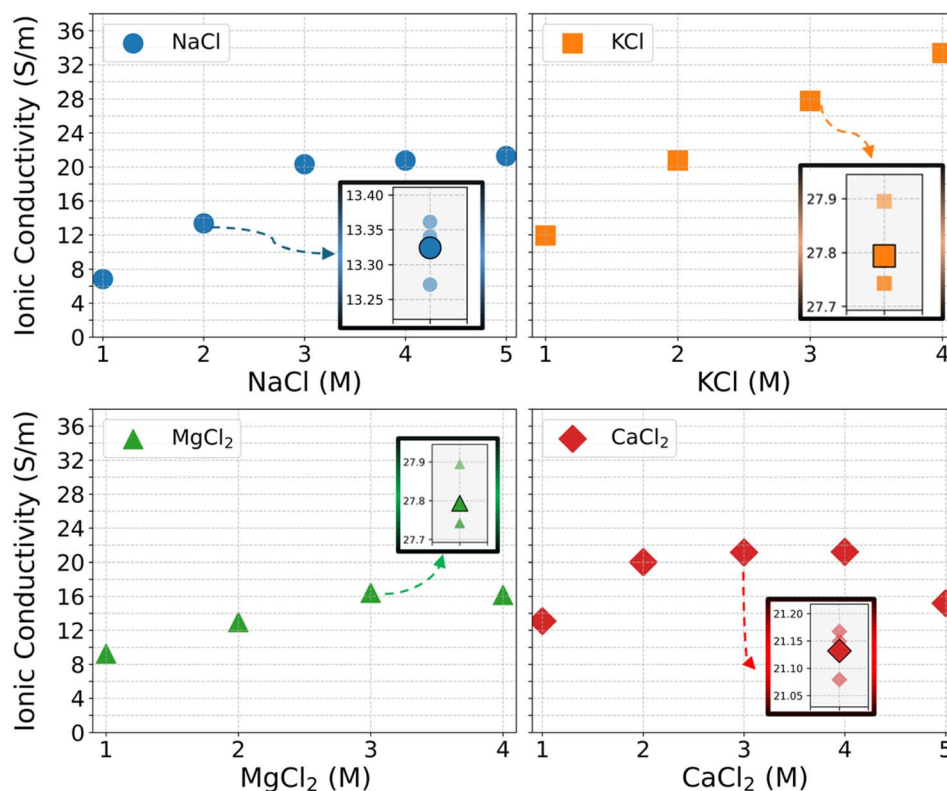


Fig. 2 Individual ionic conductivity curves of stock electrolytes (NaCl, KCl,  $\text{MgCl}_2$ ,  $\text{CaCl}_2$ ) at room temperature. Primary data are shown with solid markers, whereas lighter-colored points denote replicate experiments. Comprehensive experimental details are provided in Table S5.



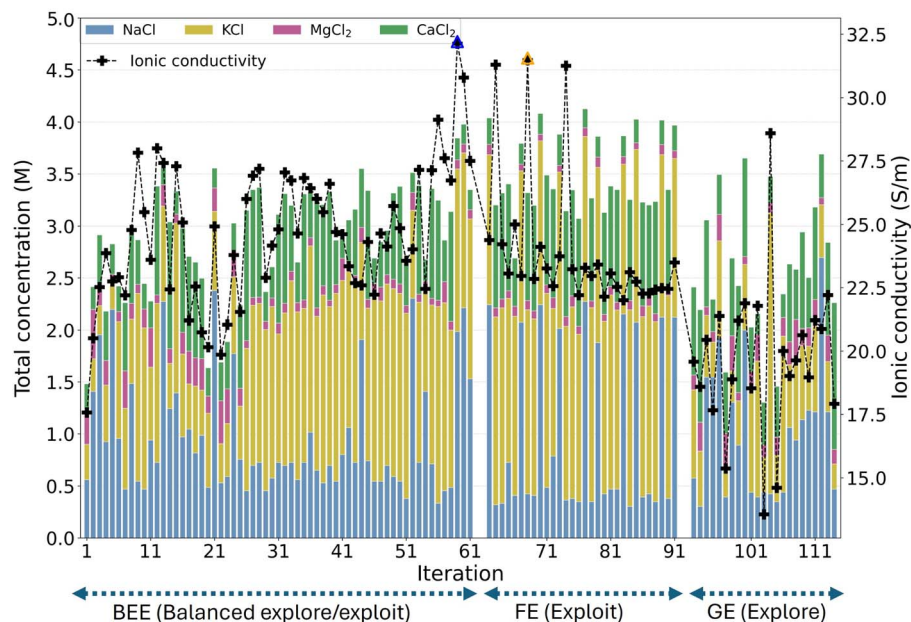


Fig. 3 Bayesian optimization of ionic conductivity in Campaign 1. Stacked bars (left axis) show total electrolyte concentration and salt fractions; the black dashed line (right axis) indicates measured conductivity. Blue and orange triangles mark the first (59) and second (68) conductivity maxima, respectively. The three BO phases (BEE, FE, GE) represent successive strategy regimes.

around a model Zn-ion battery formulation and enforced a minimum of 0.5 M  $\text{ZnCl}_2$  in every mixture. This additional requirement both narrows the composition space and challenges the optimizer to balance the sluggish mobility of  $\text{Zn}^{+2}$  with highly conductive monovalent cations. The results below show how BRINE navigated this constrained landscape to locate new conductivity optima. As shown in Fig. 4, BRINE executed 120 Bayesian-guided experiments over roughly 12 hours, going through BEE (70 runs), FE (30 runs) and GE (20 runs). Early balanced iterations revealed that  $\text{NH}_4\text{Cl}$  and KCl substantially enhanced conductivity, whereas higher  $\text{ZnCl}_2$  fractions suppressed it because of increased viscosity and ion pairing. Guided by these trends, the optimizer concentrated on  $\text{NH}_4\text{Cl}$ -rich regions during the focused phase, then broadened the search in the global phase. The highest conductivity obtained was  $28.09 \text{ S m}^{-1}$  for 0.62 M  $\text{ZnCl}_2$ , 1.03 M KCl, 1.60 M  $\text{NH}_4\text{Cl}$ , 0.21 M NaCl and 0.04 M EMIMCl; notably, this formulation emerged during the exploratory phase, underscoring the value of re-expanding the search after intensive local optimization. The second-best mixture,  $27.24 \text{ S m}^{-1}$ , contained 0.86 M  $\text{ZnCl}_2$ , 0.55 M KCl, 1.66 M  $\text{NH}_4\text{Cl}$ , 0.25 M NaCl and 0.03 M EMIMCl. Therefore,  $\text{NH}_4\text{Cl}$  consistently emerged as the dominant salt in the highest-performing mixtures, aligning with prior reports of its beneficial role in Zn-based electrolytes. Meanwhile, EMIMCl was consistently selected only at trace concentrations (0.03–0.04 M), confirming that under a conductivity-only objective it does not enhance bulk conductivity directly, while remaining relevant for future multi-objective optimization targeting interfacial stability and coulombic efficiency. Although both optima share  $\text{NH}_4\text{Cl}$  as the dominant salt, their secondary contributors differ (KCl in the global maximum and  $\text{ZnCl}_2$  in the highest local maximum), indicating multiple high-conductivity “islands” within the constrained five-component space.

Interestingly, the global maximum identified in Campaign 1 was dominated by NaCl rather than KCl, despite NaCl's lower intrinsic mobility and conductivity compared to KCl. In Campaign 2, while  $\text{NH}_4\text{Cl}$  was favored as expected,  $\text{ZnCl}_2$  generally considered a poor conductor due to sluggish ion transport, emerged as the secondary dominant salt in one optimum. These findings are not predictable from dilute-limit conductivity values or simple chemical intuition,<sup>69</sup> highlighting the importance of experimental, probability-based optimization in mapping concentrated, multicomponent electrolytes. Furthermore, BRINE identified high-conductivity regions very early in the campaigns. In Campaign 1, a formulation sampled at iteration 13 already achieved  $27.42 \text{ S m}^{-1}$ , representing  $\approx 85\%$  of the maximum ( $32.13 \text{ S m}^{-1}$ ). In Campaign 2, iteration 17 reached  $22.36 \text{ S m}^{-1}$ ,  $\approx 80\%$  of the maximum ( $28.10 \text{ S m}^{-1}$ ). In both cases, the differences in salt concentrations between the early high-performing formulations and the final maximum were within 0.02–0.69 M, showing that once BRINE located the correct basin, later iterations primarily refined compositions within a narrow sub-molar window. For further clarification, Fig. S5 plots the standalone electrolyte concentration against solution conductivity for all compositions, and Fig. S6 quantitatively depicts the aforementioned results in a scatter plot format. Moreover, Table S7 shows the comprehensive dataset, including electrolyte concentrations and ionic conductivities. We compared BRINE's optimization performance against a traditional Design of Experiments (DoE) strategy (D-optimal design). The results, presented in Note S1, Fig. S7, and Table S1, demonstrate the superior performance of BRINE when evaluated using a recently proposed benchmarking framework.<sup>70</sup>



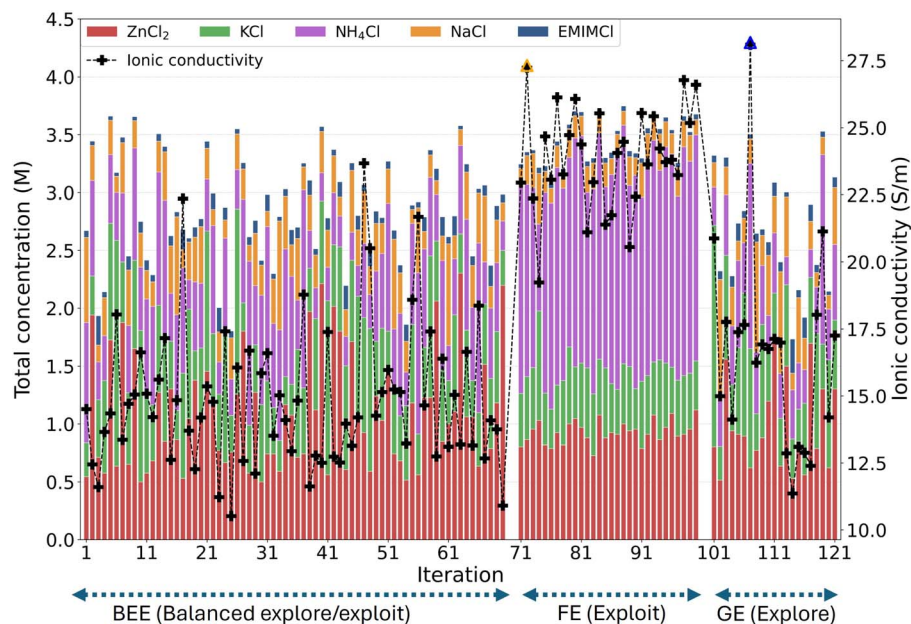


Fig. 4 Bayesian optimization of ionic conductivity in Campaign 2. Stacked bars (left axis) show total electrolyte concentration and salt fractions; the black dashed line (right axis) indicates measured conductivity. Blue and orange triangles mark the first and second conductivity maxima, respectively. The three BO phases (BEE, FE, GE) represent successive strategy regimes. Remarkably, the exploration-dominated GE phase (LCB,  $\beta = 2$ ) revealed the true global maximum.

### Validation and durability

To assess measurement stability and precision, BRINE was tasked to measure the ionic conductivity of Campaign 2's most conductive composition ( $\sigma = 32.13 \text{ S m}^{-1}$ ) by performing 15 triplicate EIS measurements alongside a manual benchmark measurement. The findings in Fig. 5 show a total SD of  $0.17 \text{ S m}^{-1}$  ( $\approx 0.6\%$ ) and a pooled within-experiment SD of  $0.05 \text{ S m}^{-1}$ , confirming high repeatability for a single electrolyte. Complementary to this, campaign-wide triplicate conductivity measurements across all compositions yielded a standard deviation within  $1 \text{ S m}^{-1}$  ( $\approx 2.5\text{--}2.8\%$  relative error; Fig. S8), providing broader validation of the workflow's reproducibility. For additional context, Table S8 compares BRINE's EIS-derived conductivities for the top-performing electrolytes from Campaigns 1 and 2 with readings from a benchtop conductivity meter (Fisherbrand Accumet AB200), showing close agreement within the instrument's tolerance range.

Phase-wise analysis shows that 80% of the conductivity gain occurred in the first forty balanced iterations. The supporting phases (Focused Exploitation and Global Exploration) added up to  $5 \text{ S m}^{-1}$  by fine-tuning the electrolyte concentrations, collectively demonstrating BRINE's ability to navigate constrained electrolyte landscapes, avoid premature convergence and identify distinct local and global optima essential for battery-grade electrolyte design (see Table S9).

To validate BRINE's optimization pipeline and quantify surrogate-model reliability, we compared Random Forest (RF) predictions with experimental conductivities and separately trained a zero-noise Gaussian Process (GP) on the full data set. Fig. 6 overlays RF-predicted conductivity surfaces and associated uncertainty maps for the most influential salt pairs from

each campaign, KCl–CaCl<sub>2</sub> for Campaign 1 and NH<sub>4</sub>Cl–ZnCl<sub>2</sub> for Campaign 2, while all remaining salts are fixed at their experimentally determined optima. In both cases, the RF model places the global or local maximum within  $0.25 \text{ M}$  of the measured peak, and prediction uncertainty ( $\sigma_u$ ) falls below  $2 \text{ S m}^{-1}$  in these neighborhoods, indicating confident interpolation near the optima. The GP mean surface (Fig. S9) reproduces the RF maxima to within  $0.4 \text{ S m}^{-1}$  and yields a root-mean-square error  $< 4\%$ , confirming that model choice does not affect the location or magnitude of the conductivity peaks.

Together, these results demonstrate that (i) the RF surrogate provides accurate, low-uncertainty guidance throughout the Bayesian search, (ii) the GP cross-check corroborates RF predictions, and (iii) BRINE's automated measurements are repeatable and reproducible, confirming the platform's reliability for data-driven electrolyte research. It is noteworthy that when compared with dilute-limit predictions from Kohlrausch's law, Campaign 1 optimum exhibited  $a \approx 45\%$  reduction in conductivity relative to the additive estimate, confirming the strong non-ideal transport effects present in these systems (see SI for detailed calculations).

### BRINE limitations and improvements

Despite its demonstrated capabilities, BRINE faces several constraints. Experiments lasting longer than two days risk solvent evaporation, which can alter stock concentrations and require replenishment. Environmental fluctuations in temperature and humidity may also introduce variability in EIS measurements; therefore, extended campaigns would benefit from operation inside a controlled environmental chamber.



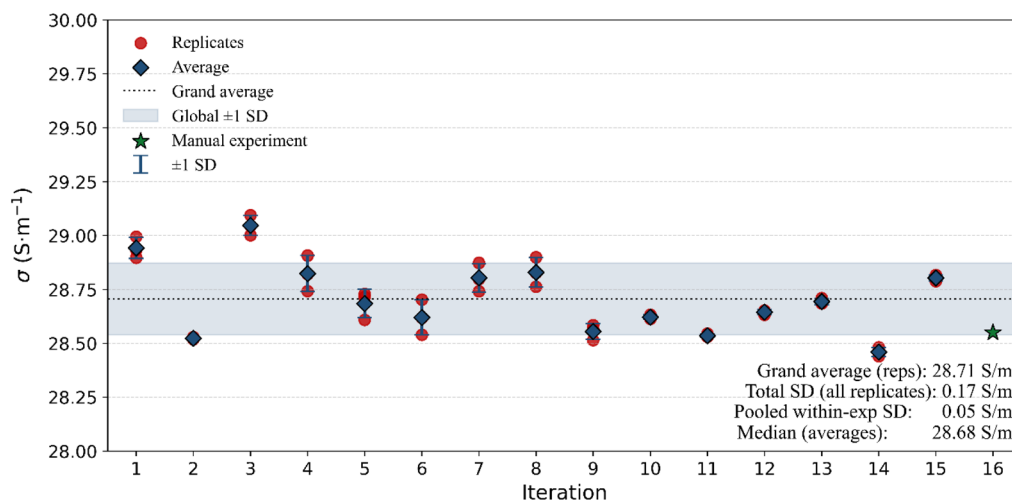


Fig. 5 Reproducibility of conductivity measurements. Red points represent the results of replicate measurements, and blue diamonds indicate replicate averages per iteration. BRINE achieved a grand average conductivity of  $28.71 \text{ S m}^{-1}$  with a total standard deviation (SD, all data points) of  $0.17 \text{ S m}^{-1}$  and a pooled within-experiment SD of  $0.05 \text{ S m}^{-1}$ . A manually prepared sample, measured via EIS using the same Pt||Pt electrode setup and potentiostat, yielded  $28.55 \text{ S m}^{-1}$  (green star), in close agreement with the automated results. See Note S2 for detailed equations.

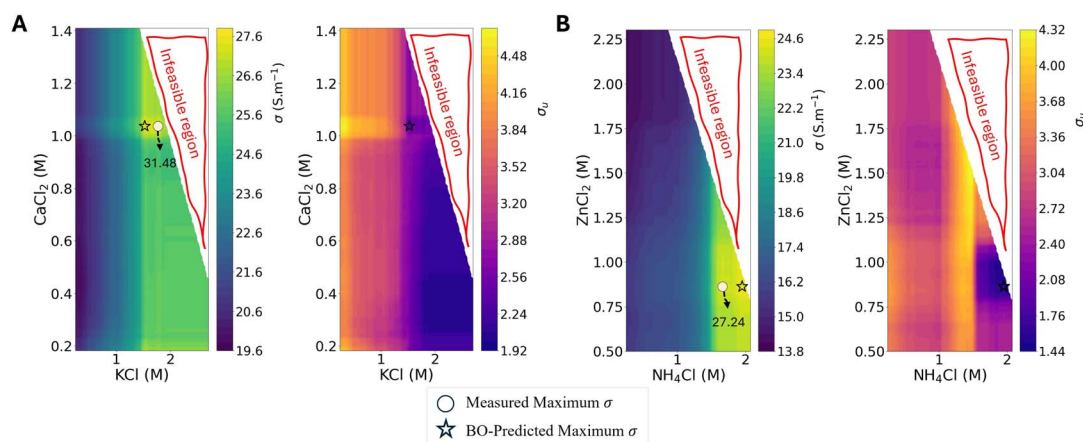


Fig. 6 Random forest-based Bayesian optimization (BO) conductivity predictions for selected electrolyte pairs. Campaign 1 (A): KCl and  $\text{CaCl}_2$ ; Campaign 2 (B):  $\text{NH}_4\text{Cl}$  and  $\text{ZnCl}_2$ . Color scales represent BO-predicted conductivity ( $\sigma$ , left plot in each pair) and prediction uncertainty ( $\sigma_u$ , right plot in each pair). Red contours indicate regions exceeding volume constraints (infeasible region). Star markers represent predicted (Bayesian) and measured (experimental) conductivity maxima. Predictions align closely ( $<0.25 \text{ M}$  deviation) with experimental measurements, demonstrating accurate and confident surrogate modelling near optimal conditions.

In its current configuration, BRINE is only capable of performing EIS measurements. While the electrode assembly is compatible with a suite of other electrochemical techniques, additional scripts and analysis workflows would need to be developed. Planned upgrades include new electrode assemblies, cell designs, and protocols for cyclic voltammetry, linear sweep voltammetry, chronopotentiometry, and chronoamperometry in both two- and three-electrode setups. These improvements will be reported in our future publications.

BRINE also has several hardware constraints. The OT-2 deck space limits the number of available cells, and extending experimental sequences would require additional automation, such as integration with a robotic arm. Pipetting resolution further imposes a lower bound on the concentrations accessible from stock solutions. This limitation did not prevent

identification of global optima when relatively few inputs ( $<7$ ) were explored, partly because electrolyte conductivity tends to increase at medium to high concentrations. However, as the number of salts increases, the fraction range of each component becomes smaller, causing more concentration ranges to fall into infeasible regions and increasing the risk of the Bayesian optimizer being confined to local maxima. Strategies to mitigate this include preparing multiple stock solutions at varying concentrations, using custom-made well plates with larger wells, or employing advanced programmable pipettes.

## Conclusions

BRINE is an open-source electrochemical self-driving laboratory capable of autonomously exploring multicomponent electrolyte





spaces to identify high-performance mixed electrolytes with both speed and reliability. Across two closed-loop Bayesian campaigns, the platform screened more than 230 unique formulations in under 20 hours, achieving conductivities of  $32.12 \text{ S m}^{-1}$  in an unconstrained four-salt system and  $28.09 \text{ S m}^{-1}$  when a  $0.5 \text{ M ZnCl}_2$  constraint was imposed. Random Forest and Gaussian Process surrogates located experimental optima within  $\pm 0.25 \text{ M}$ , while repeated EIS measurements demonstrated a total standard deviation of only  $0.17 \text{ S m}^{-1}$  ( $\approx 0.6\%$ ), confirming high precision and measurement reliability. Although the present study focused on ionic conductivity, BRINE's modular hardware and Python control architecture can readily accommodate other electrochemical techniques, such as cyclic voltammetry, galvanostatic cycling, and linear sweep voltammetry, enabling comprehensive optimization of electrolyte properties for specific battery chemistries. Future work will leverage these expanded capabilities to identify application-tailored electrolytes that balance conductivity, electrochemical stability, and interfacial compatibility, positioning BRINE as a versatile foundation for future data-driven electrolyte discovery.

## Conflicts of interest

The authors declare no conflicts.

## Data availability

Data for this article, including the Python codes used to orchestrate and control BRINE, Bayesian-optimization workflows, CAD files, and electrode setup designs, are available at Zenodo at <https://doi.org/10.5281/zenodo.17715201>. See supplementary information (SI) for additional details. Supplementary information: the full experimental datasets from experimental campaigns, additional notes and methodological clarifications, supporting figures, and a short demonstration video. It also provides links to the associated GitHub repository containing auxiliary scripts. See DOI: <https://doi.org/10.1039/d5dd00353a>.

## Acknowledgements

The authors gratefully acknowledge support from the National Science Foundation under Award No. 2403874.

## References

- 1 H. Quinn, G. A. Robben, Z. Zheng, A. L. Gardner, J. G. Werner and K. A. Brown, *Mater. Horiz.*, 2024, **11**, 5331–5340.
- 2 K. Khan, A. K. Tareen, M. Aslam, Y. Zhang, R. Wang, Z. Ouyang, Z. Gou and H. Zhang, *Nanoscale*, 2019, **11**, 21622–21678.
- 3 M. Shoaib, P. Vallayil, N. Jaiswal, P. Iyapazham Vaigunda Suba, S. Sankararaman, K. Ramanujam and V. Thangadurai, *Adv. Energy Mater.*, 2024, **14**, 2400721.
- 4 D. G. Kwabi, Y. Ji and M. J. Aziz, *Chem. Rev.*, 2020, **120**, 6467–6489.
- 5 A. M. Fenton, R. K. Jha, B. J. Neyhouse, A. P. Kaur, D. A. Dailey, S. A. Odom and F. R. Brushett, *J. Mater. Chem. A*, 2022, **10**, 17988–17999.
- 6 A. Barai, K. Uddin, W. D. Widanage, A. McGordon and P. Jennings, *Sci. Rep.*, 2018, **8**, 21.
- 7 Q. Zhao, S. Stalin, C.-Z. Zhao and L. A. Archer, *Nat. Rev. Mater.*, 2020, **5**, 229–252.
- 8 J. C. Bachman, S. Muy, A. Grimaud, H.-H. Chang, N. Pour, S. F. Lux, O. Paschos, F. Maglia, S. Lupart, P. Lamp, L. Giordano and Y. Shao-Horn, *Chem. Rev.*, 2016, **116**, 140–162.
- 9 M. Libber, N. Gariya and M. Kumar, *J. Solid State Electrochem.*, 2025, **29**, 513–527.
- 10 M. Shahzad, F. Ahmad, M. Ibraheem, A. Shakoor, S. M. Ramay, M. R. Raza and S. Atiq, *RSC Adv.*, 2025, **15**, 6308–6323.
- 11 W. Feng, B. Chang, Y. Ren, D. Kong, H. B. Tao, L. Zhi, M. A. Khan, R. Aleisa, M. Rueping and H. Zhang, *Adv. Mater.*, 2025, **37**, 2416012.
- 12 C. Gervill  -Mouravieff, W. Bao, D. A. Steingart and Y. S. Meng, *Nat. Rev. Electr. Eng.*, 2024, **1**, 547–558.
- 13 Y. Song, J. Ju, J. Wang, K. Li, X. Wang, R. Gao, H. Lu, D. Chao and Y. Wang, *Adv. Mater.*, 2025, **37**, 2500941.
- 14 G. Smith and E. J. F. Dickinson, *Nat. Commun.*, 2022, **13**, 6832.
- 15 A. Moradpour, M. Kasper, J. Hoffmann and F. Kienberger, *IEEE Trans. Instrum. Meas.*, 2022, **71**, 1–9.
- 16 R. Dugas, J. D. Forero-Saboya and A. Ponrouch, *Chem. Mater.*, 2019, **31**, 8613–8628.
- 17 L. Liu, Z.-J. Chen, G.-Y. Zhu, B.-H. Huang, B. Wang, Y. Yao, D.-S. Bin, X. Rui and Y. Yu, *Energy Environ. Sci.*, 2025, **18**, 2668–2685.
- 18 Z. Huang, Z. Xiao, R. Jin, Z. Li, C. Shu, R. Shi, X. Wang, Z. Tang, W. Tang and Y. Wu, *Energy Environ. Sci.*, 2024, **17**, 5365–5386.
- 19 H. Ahn, D. Kim, M. Lee and K. W. Nam, *Commun. Mater.*, 2023, **4**, 37.
- 20 S. Naseri Boroujeni, B. Maribo-Mogensen, X. Liang and G. M. Kontogeorgis, *J. Phys. Chem. B*, 2024, **128**, 536–550.
- 21 W. Zhang, X. Chen, Y. Wang, L. Wu and Y. Hu, *ACS Omega*, 2020, **5**, 22465–22474.
- 22 S. Matsuda, G. Lambard and K. Sodeyama, *Cell Rep. Phys. Sci.*, 2022, **3**, 100832.
- 23 S. Sadeghi, R. B. Canty, N. Mukhin, J. Xu, F. Delgado-Licona and M. Abolhasani, *ACS Sustain. Chem. Eng.*, 2024, **12**, 12695–12707.
- 24 S. Dolo  , M. Das, Y. Li, Z. H. Cho, X. Xiao, J. V. Hanna, M. Osvaldo and L. Ng Wei Tat, *Digital Discovery*, 2025, **4**, 1685–1721.
- 25 J. Qiu, L. Zhu, Z. Feng, Z. Luo and L. Wang, *Chem. Commun.*, 2025, **61**, 10026–10038.
- 26 M. Sim, M. G. Vakili, F. Strieth-Kalthoff, H. Hao, R. J. Hickman, S. Miret, S. Pablo-Garc  a and A. Aspuru-Guzik, *Matter*, 2024, **7**, 2959–2977.
- 27 J. Li, J. Li, R. Liu, Y. Tu, Y. Li, J. Cheng, T. He and X. Zhu, *Nat. Commun.*, 2020, **11**, 2046.



- 28 H. Quinn, G. A. Robben, Z. Zheng, A. L. Gardner, J. G. Werner and K. A. Brown, *Mater. Horiz.*, 2024, **11**, 5331–5340.
- 29 F. Rahmanian, J. Flowers, D. Guevarra, M. Richter, M. Fichtner, P. Donnelly, J. M. Gregoire and H. S. Stein, *Adv. Mater. Interfaces*, 2022, **9**, 2101987.
- 30 A. Al-Najjar, N. S. V. Rao, C. A. Bridges, S. Dai and A. Walters, in *2024 IEEE 20th International Conference on e-Science (e-Science)*, IEEE, Osaka, Japan, 2024, pp. 1–10.
- 31 A. Vriza, H. Chan and J. Xu, *Chem. Mater.*, 2023, **35**, 3046–3056.
- 32 M. Seifrid, R. Pollice, A. Aguilar-Granda, Z. Morgan Chan, K. Hotta, C. T. Ser, J. Vestfrid, T. C. Wu and A. Aspuru-Guzik, *Acc. Chem. Res.*, 2022, **55**, 2454–2466.
- 33 S. Lo, S. G. Baird, J. Schrier, B. Blaiszik, N. Carson, I. Foster, A. Aguilar-Granda, S. V. Kalinin, B. Maruyama, M. Politi, H. Tran, T. D. Sparks and A. Aspuru-Guzik, *Digital Discovery*, 2024, **3**, 842–868.
- 34 K. L. Snapp and K. A. Brown, *Digital Discovery*, 2023, **2**, 1620–1629.
- 35 S. Naseri Boroujeni, B. Maribo-Mogensen, X. Liang and G. M. Kontogeorgis, *J. Phys. Chem. B*, 2023, **127**, 9954–9975.
- 36 W. Zhang, X. Chen, Y. Wang, L. Wu and Y. Hu, *ACS Omega*, 2020, **5**, 22465–22474.
- 37 Y. Avni, D. Andelman and H. Orland, *J. Chem. Phys.*, 2022, **157**, 154502.
- 38 J. K. Pedersen, C. M. Clausen, O. A. Krysiak, B. Xiao, T. A. A. Batchelor, T. Löffler, V. A. Mints, L. Banko, M. Arenz, A. Savan, W. Schuhmann, A. Ludwig and J. Rossmeisl, *Angew. Chem.*, 2021, **133**, 24346–24354.
- 39 G. Tom, S. P. Schmid, S. G. Baird, Y. Cao, K. Darvish, H. Hao, S. Lo, S. Pablo-García, E. M. Rajaonson, M. Skreta, N. Yoshikawa, S. Corapi, G. D. Akkoc, F. Strieth-Kalthoff, M. Seifrid and A. Aspuru-Guzik, *Chem. Rev.*, 2024, **124**, 9633–9732.
- 40 J. T. Yik, L. Zhang, J. Sjölund, X. Hou, P. H. Svensson, K. Edström and E. J. Berg, *Digital Discovery*, 2023, **2**, 799–808.
- 41 J. T. Yik, C. Hvarfner, J. Sjölund, E. J. Berg and L. Zhang, *Cell Rep. Phys. Sci.*, 2025, **6**, 102548.
- 42 D.-Z. Lin, K.-J. Pan, Y. Li, C. B. Musgrave Iii, L. Zhang, K. N. Jayarapu, T. Li, J. V. Tran, W. A. Goddard, Z. Luo and Y. Liu, *Sci. Adv.*, 2025, **11**, eadu4391.
- 43 R. Sinmyo and H. Keppler, *Contrib. Mineral. Petrol.*, 2017, **172**, 4.
- 44 A. J. Lucio, I. Sumarlan, E. Bulmer, I. Efimov, S. Viles, A. R. Hillman, C. J. Zaleski and K. S. Ryder, *J. Phys. Chem. C*, 2023, **127**, 13866–13876.
- 45 Y.-H. Liu, Y. Yu, Y. Zhang, Z.-Y. Hu, X.-L. Lv, L. Lin and W.-Q. Liu, *J. Phys. Chem. Lett.*, 2025, **16**, 8936–8945.
- 46 Y.-X. Liu, T.-Y. Kan, Y.-H. Hsieh, Y.-Y. Ho, Y.-H. Chang, Y.-M. Weng, C.-H. Yang, C.-X. Yu, T.-C. Hsu, Y.-H. Huang, Y.-T. Tsai, C.-C. Hsu, C.-C. Hua, Y.-Y. Li, H.-W. Chang and Y.-C. Fu, *J. Taiwan Inst. Chem. Eng.*, 2025, **167**, 105909.
- 47 W. Zhang, Y. Dai, R. Chen, Z. Xu, J. Li, W. Zong, H. Li, Z. Li, Z. Zhang, J. Zhu, F. Guo, X. Gao, Z. Du, J. Chen, T. Wang, G. He and I. P. Parkin, *Angew. Chem., Int. Ed.*, 2023, **62**, e202212695.
- 48 J. Meng, Y. Song, J. Wang, P. Hei, C. Liu, M. Li, Y. Lin and X.-X. Liu, *Chem. Sci.*, 2024, **15**, 220–229.
- 49 Y.-L. Zhao, M. Meot-Ner (Mautner) and C. Gonzalez, *J. Phys. Chem. A*, 2009, **113**, 2967–2974.
- 50 A. Behera, D. Deb and A. J. Bhattacharyya, *J. Mater. Chem. A*, 2025, **13**, 33784–33797.
- 51 C. Shen, Y. Zhang, X. Li, P. Guo, X. Zeng, K. Ni, R. Cao, Z. Wang, Z. Wang and L. Qin, *J. Mater. Chem. A*, 2025, **13**, 2174–2186.
- 52 Z. Guan, L. Bai and B. Du, *Materials*, 2023, **16**, 7504.
- 53 J. Liu, Z. Peng, R. Liao, J. Zhou and Q. Zhang, *Batter. Supercaps*, 2025, 202500420.
- 54 S. S. Manna, P. Bhauriyal and B. Pathak, *Mater. Adv.*, 2020, **1**, 1354–1363.
- 55 N. F. Mazuki and A. S. B. Samsudin, *Mol. Cryst. Liq. Cryst.*, 2023, **759**, 53–69.
- 56 V. Yrjänä, *J. Open Source Softw.*, 2022, **7**, 4808.
- 57 R. Tamura, K. Tsuda and S. Matsuda, *Sci. Technol. Adv. Mater. Methods*, 2023, **3**, 2232297.
- 58 I. Fette and A. Melnikov, *The WebSocket Protocol*, RFC Editor, 2011.
- 59 W. Ouyang, R. W. Bowman, H. Wang, K. E. Bumke, J. T. Collins, O. Spjuth, J. Carreras-Puigvert and B. Diederich, *Adv. Biol.*, 2022, **6**, 2101063.
- 60 M. Lindauer, K. Eggensperger, M. Feurer, A. Biedenkapp, D. Deng, C. Benjamins, T. Ruhkopf, R. Sass and F. Hutter, *J. Mach. Learn. Res.*, 2022, **23**, 1–9.
- 61 W. Zhang, C. Wu, H. Zhong, Y. Li and L. Wang, *Geosci. Front.*, 2021, **12**, 469–477.
- 62 Y.-F. Lim, C. K. Ng, U. S. Vaitesswar and K. Hippalgaonkar, *Adv. Intell. Syst.*, 2021, **3**, 2100101.
- 63 E. Brochu, M. W. Hoffman and N. de Freitas, *arXiv*, 2010, DOI: [10.48550/ARXIV.1009.5419](https://doi.org/10.48550/ARXIV.1009.5419).
- 64 A. Dave, J. Mitchell, S. Burke, H. Lin, J. Whitacre and V. Viswanathan, *Nat. Commun.*, 2022, **13**, 5454.
- 65 S. Zhang, F. Yang, C. Yan, D. Zhou and X. Zeng, *IEEE Trans. Comput.-Aided Des. Integr. Circuits Syst.*, 2022, **41**, 1–14.
- 66 T. D. P. Vasconcelos, D. A. De Souza, G. C. D. M. Virgolino, C. L. C. Mattos and J. P. P. Gomes, *Expert Syst. Appl.*, 2022, **188**, 115847.
- 67 M. Micari, M. Bevacqua, A. Cipollina, A. Tamburini, W. Van Baak, T. Putts and G. Micala, *J. Membr. Sci.*, 2018, **551**, 315–325.
- 68 J. Shaw-Stewart, A. Alvarez-Reguera, A. Greszta, J. Marco, M. Masood, R. Sommerville and E. Kendrick, *Sustain. Mater. Technol.*, 2019, **22**, e00110.
- 69 Y. Avni, R. M. Adar, D. Andelman and H. Orland, *Phys. Rev. Lett.*, 2022, **128**, 098002.
- 70 A. D. Adesiji, J. Wang, C.-S. Kuo and K. A. Brown, *Digital Discovery*, 2026, DOI: [10.1039/D5DD00037G](https://doi.org/10.1039/D5DD00037G).

